



**HAL**  
open science

## **Pulsewidth-switchable ultrafast source at 114 nm**

Anahita Omoumi, Michele Natile, Evangelos Papalazarou, Yoann Zaouter,  
Thierry Auguste, Marc Hanna, Patrick Georges, Marino Marsi

► **To cite this version:**

Anahita Omoumi, Michele Natile, Evangelos Papalazarou, Yoann Zaouter, Thierry Auguste, et al..  
Pulsewidth-switchable ultrafast source at 114 nm. *Optics Letters*, 2023, 48 (17), pp.4625-4628.  
10.1364/OL.498266 . hal-04192119

**HAL Id: hal-04192119**

**<https://hal-iogs.archives-ouvertes.fr/hal-04192119>**

Submitted on 31 Aug 2023

**HAL** is a multi-disciplinary open access archive for the deposit and dissemination of scientific research documents, whether they are published or not. The documents may come from teaching and research institutions in France or abroad, or from public or private research centers.

L'archive ouverte pluridisciplinaire **HAL**, est destinée au dépôt et à la diffusion de documents scientifiques de niveau recherche, publiés ou non, émanant des établissements d'enseignement et de recherche français ou étrangers, des laboratoires publics ou privés.

# Pulsewidth-switchable ultrafast source at 114 nm

ANAHITA OMOUMI<sup>1,2,3,\*</sup>, MICHELE NATILE<sup>3</sup>, EVANGELOS PAPALAZAROU<sup>2</sup>, YOANN ZAOUTER<sup>3</sup>, THIERRY AUGUSTE<sup>4</sup>, MARC HANNA<sup>1</sup>, PATRICK GEORGES<sup>1</sup>, AND MARINO MARSI<sup>2</sup>

<sup>1</sup> Université Paris-Saclay, Institut d'Optique Graduate School, CNRS, Laboratoire Charles Fabry, 91127 Palaiseau Cedex, France

<sup>2</sup> Université Paris-Saclay, Laboratoire de Physique des solides, 91400 Orsay Cedex, France

<sup>3</sup> Amplitude, 11 Avenue de Canteranne, Cité de la Photonique, 33600 Pessac, France

<sup>4</sup> Université Paris-Saclay, CEA, CNRS, Laboratoire Interactions Dynamiques et Lasers, 91191 Gif-sur-Yvette, France

\* [anahita.omoumi@universite-paris-saclay.fr](mailto:anahita.omoumi@universite-paris-saclay.fr)

Compiled August 7, 2023

Femtosecond laser sources with high repetition rate are fundamental tools enabling tabletop time-resolved and angle-resolved photoemission spectroscopy in solids. The UV and vacuum UV laser light required for the photoemission process can be generated through various frequency up-conversion techniques. We describe a VUV source at 114 nm (10.8 eV) based on an industrial grade ytterbium-doped ultrafast laser, a nonlinear pulsewidth selection stage, and two cascaded frequency tripling stages, first in crystals, second in xenon. The role of ionization in gas-based perturbative third harmonic generation phase-matching is analyzed using a simple theory, numerical simulations, and experimental data. The source features high photon flux, high repetition rate and adjustable time resolutions. Thereby, in combination with a state-of-the-art ARPES apparatus it enables the study of the electronic dynamics of the whole Brillouin zone in a large number of materials. ©

2023 Optica Publishing Group

<http://dx.doi.org/10.1364/ao.XX.XXXXXX>

The rapid expansion of femtosecond laser sources with high repetition rate considerably increases the performance of a number of spectroscopy techniques, including tabletop time-resolved and angle-resolved photoemission spectroscopy (tr-ARPES) in solids. tr-ARPES is an instrumental technique in condensed matter physics which enables access to the band structure of solids as well as exploring the dynamics of quasiparticles in quantum materials [1]. The characteristics of the light source used to generate photoelectrons largely determine the performances of any tr-ARPES experiment. For instance, the achievable time and momentum/energy resolutions are related to the optical pulsewidth and bandwidth, the achievable signal to noise ratio and acquisition time are related to the repetition rate and photon flux of the source, and the accessible momentum space is determined by its central wavelength. To efficiently probe the materials, vacuum ultraviolet (VUV) or extreme-ultraviolet (EUV) ultrafast sources are required. UV light at energies around 6 eV overcomes the work function of solids and is extensively used as probe in tr-ARPES [2] but it can detect only electronic

states in the proximity of the Gamma point. In order to access the whole Brillouin zone, higher energy photons are necessary.

Besides synchrotron and free-electron laser facilities, with limited access, tabletop sources based on frequency up-conversion of ultrafast lasers in the near infrared have been developed for this purpose. Depending on the up-conversion mechanism, these can be classified in two categories. First, some sources are based on non-perturbative high-harmonic generation (HHG) [3, 4], which allows access to the EUV range in a single step, often with limited photon flux and spectral resolution. Second, multiple stages of perturbative nonlinear processes can be performed to access the VUV range [5, 6], first in crystals for wavelengths above  $\sim 200$  nm, then in gases. The technology shift from titanium-doped sapphire lasers to ytterbium-based lasers has allowed an increase in repetition rate of these tabletop VUV sources and triggered renewed interest to optimize them for tr-ARPES. In particular, cascaded frequency tripling of high power laser systems at a central wavelength of  $\sim 1$   $\mu$ m has been investigated [7–10]. In these sources a first stage of third-harmonic generation (THG) is performed using second-harmonic generation (SHG) and sum-frequency generation (SFG) in nonlinear crystals. This is followed by a second THG stage in a rare gas or gas mixture which is a third-order perturbative nonlinear effect subject to phase matching (PM).

Here, we describe a high repetition rate VUV source based on cascaded frequency tripling of Fourier transform-limited (FTL) pulses with a duration easily switchable between 100 fs, 500 fs, and 3 ps. The 500 fs pulses delivered by the driving ytterbium-based laser at 1030 nm and 100 kHz can be used directly or sent to a nonlinear multipass cell (MPC) that performs either spectral broadening or spectral compression, depending on the input chirp. The pulses are then sent to a first crystal-based THG stage, then focused in a xenon cell to generate the ninth harmonic.

This unique setup allows us to observe and analyze the dependence of PM pressure on experimental parameters such as pulsewidth, intensity, and focusing conditions. In particular, although THG in gases has been observed and used for decades [11], the effect of ionization on the process phase-matching has not been considered in detail, in contrast with HHG. We provide such an analysis and show that it matches the experimentally observed THG efficiency as a function of gas pressure and pulsewidth. The versatility of this source at 114 nm (10.8 eV)

in terms of spectral/temporal width, combined with a photon flux in the  $10^{12}$  ph/s range makes it very appealing for various tr-ARPES experiments.

We first analyze the influence of ionization in the PM of perturbative gas-based THG. Early analyses of this problem [11–13] establish the possibility to obtain PM conditions by compensating neutral gas dispersion by the Gouy phase. To include analytically the effect of ionization, we turn to a description localized in one plane, similar to what is done in HHG [14, 15]. In the following, we assume that this plane corresponds to the driving pulse waist. In contrast to HHG, in the perturbative THG case, the atomic dipole phase is not relevant. Including contributions from neutral atoms, self- and cross-phase modulation (SPM, XPM) induced by the fundamental, Gouy phase, and free electrons, the phase mismatch  $\Delta k = k_{3\omega} - 3k_{\omega}$  can be written as

$$\Delta k = \frac{\Omega}{c} [(n_{3\omega} - n_{\omega}) + (n_{2X} - n_{2S}) I_{\omega}] + \frac{2}{z_R} + \frac{4e^2 n_e}{\Omega m_e \epsilon_0 c}, \quad (1)$$

where  $\Omega = 3\omega$  is the angular frequency of the third harmonic,  $n_{\omega}$  and  $n_{3\omega}$  are the refractive indices at the fundamental and third harmonic wavelengths,  $c$  is the speed of light,  $z_R$  is the Rayleigh range,  $I_{\omega}$  is the intensity of the fundamental,  $n_{2X}$  is the nonlinear index associated with XPM from the fundamental onto the third harmonic,  $n_{2S}$  is the nonlinear index governing SPM of the fundamental,  $e$ ,  $m_e$ , and  $n_e$  are the electron charge, mass, and density, and  $\epsilon_0$  is the vacuum permittivity. At 343 nm, for intensities below  $5 \times 10^{13}$  W/cm<sup>2</sup> in xenon, ionization is well approximated by a three-photon process. Assuming a low ionization fraction and a Gaussian pulse profile, the electron density at the peak of the pulse is given by [16]

$$n_e = \frac{1}{4} n_0 \sigma_3 I_{\omega}^3 \sqrt{\frac{\pi}{3 \ln 2}} \Delta t, \quad (2)$$

where  $n_0$  is the initial atomic density, and  $\Delta t$  is the Full Width at Half Maximum (FWHM) pulsewidth. The three-photon ionization cross-section of xenon  $\sigma_3 \approx 1.2 \times 10^{-39} (\text{W}\cdot\text{m}^{-2})^{-3} \cdot \text{s}^{-1}$  is found by fitting ionization rates calculated using the method described in [17] in the multiphoton regime. Substituting this expression in Eq. (1), and removing the SPM/XPM term, which is found to be negligible in our conditions (two orders of magnitude lower than the neutral atoms contribution for  $I_{\omega} = 10^{13}$  W.cm<sup>-2</sup>), the phase mismatch can be written as

$$\Delta k = \frac{\Omega}{c} p_{Xe} \Delta N_{Xe} + \frac{2}{z_R} + \kappa p_{Xe} \Delta t I^3 \quad (3)$$

$$\kappa = \frac{e^2 n_L \sigma_3}{\Omega m_e \epsilon_0 c} \sqrt{\frac{\pi}{3 \ln 2}}$$

where  $n_L$  is the Loschmidt constant,  $p_{Xe}$  is the xenon pressure, the refractive indices have been written as  $n_{\omega, 3\omega} = 1 + p_{Xe} N_{\omega, 3\omega}$  to bring forward their linear pressure dependence, and  $\Delta N_{Xe} = N_{3\omega} - N_{\omega} \approx -3.7 \times 10^{-4} \text{ bar}^{-1}$ . Setting  $\Delta k = 0$  allows us to find a relationship between the PM pressure and the intensity

$$I_{\omega}^3 = -\frac{1}{\kappa \Delta t} \left( \frac{\Omega}{c} \Delta N_{Xe} + \frac{2}{z_R p_{Xe}} \right). \quad (4)$$

The first term in the parenthesis, corresponding to the neutral dispersion, is negative, while the second one, corresponding to the Gouy phase, is positive. Figure 1 illustrates this relationship at a driving wavelength of 343 nm in xenon for three focusing conditions and pulse durations. When ionization is negligible

( $I \rightarrow 0$ ), we recover the balance between neutral dispersion and Gouy phase, defining a first horizontal asymptote.

$$z_R p_{Xe} = -2 \frac{c}{\Omega \Delta N_{Xe}}. \quad (5)$$

As the intensity increases, the PM pressure increases because the neutral atoms dispersion must compensate for the ionization contribution. At high intensity the neutral atoms dispersion contribution must be much higher than the Gouy phase contribution to balance ionization, leading to a second vertical asymptote

$$I_{\omega}^3 = -\frac{1}{\kappa \Delta t} \frac{\Omega}{c} \Delta N_{Xe}. \quad (6)$$

The horizontal asymptote moves up to a higher pressure when the waist radius is decreased, and the vertical asymptote is shifted to a higher intensity when reducing the pulse duration. As in the case of HHG [15], shorter pulsewidths allow the possibility of phase-matching over a larger intensity range, because the peak intensity can be reached for a lower ionization fraction.

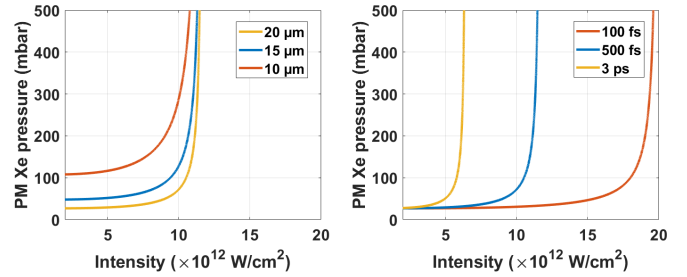


**Fig. 1.** PM pressure as a function of intensity of the driving pulse at 343 nm in the Xe cell. Left: different waist radii at fixed 500 fs pulse duration. Right: different pulse durations at fixed waist radius of 10  $\mu\text{m}$ .

To capture physical effects beyond this simplified analysis, that considers phase-matching in a single plane at maximum intensity in space and time, we compare the experimental results with numerical simulations. These simulations are based on solving two coupled envelope equations for the fundamental and THG fields in (2+1)D geometry ( $r, z, t$ ), assuming radial symmetry. They take into account diffraction, dispersion through a Sellmeier equation for xenon [13], THG, SPM, XPM, assuming a single  $\chi^{(3)}$  value corresponding to a nonlinear index  $n_2 = 5.2 \times 10^{-23} \text{ m}^2/\text{W}$  for all these processes, and ionization-related effects including free electron dispersion. This model allows to get a more accurate picture, taking into account the temporal, transverse and longitudinal spatial variations in intensity and phase for both beams. For comparison with experiments, the only slightly adjusted parameter is the waist radius, because it was difficult to estimate its precise value due to the limited resolution of the camera used.

We now turn to the description of the experimental setup, shown in Fig. 2. It starts with an Yb-doped industrial laser source (Tangor, Amplitude) that delivers 500 fs 300  $\mu\text{J}$  pulses at 100 kHz repetition rate and 1030 nm wavelength. This laser is delivered with a remote-controlled grating-based compressor unit that allows easy chirp adjustment of the output pulses. Using a set of flip mirrors, the pulses can either be sent directly to the crystal-based frequency tripling stage to seed the 500 fs beam-line, or to a MPC to manipulate the pulse duration. This MPC is

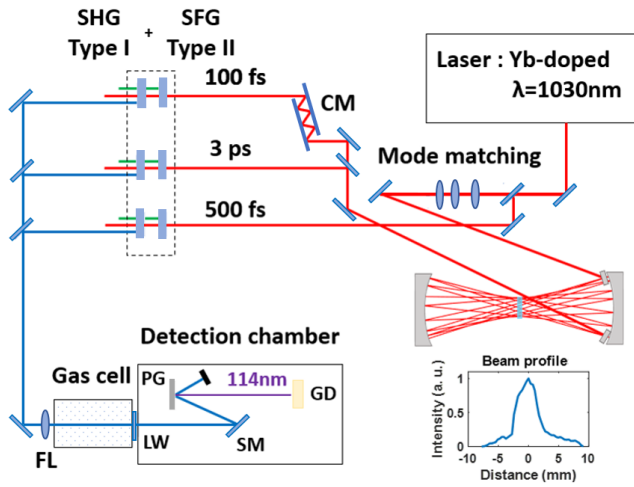


**Fig. 2.** GD: gold detector, SM: spherical mirror, PG: plane grating, LW: LiF window, FL: focusing lens, CM: chirped mirrors. Layout of the experimental setup. Inset: beam profile of the 114 nm pulses based on a knife edge measurement after the grating.

143 designed so that, if the input pulses are FTL, it compresses them  
 144 down to 100 fs [18, 19], while if they are negatively stretched  
 145 to 3 ps, it compresses the spectrum down to the FTL limit [20].  
 146 Indeed, applying self-phase modulation on negatively chirped  
 147 pulses results in instantaneous frequency shifts that suppress  
 148 the edges of the input spectrum. This results in a very easy  
 149 switch between 100 fs (temporal compression), 500 fs (initial  
 150 laser source), and 3 ps (spectral compression) FTL pulses.

151 The MPC is composed of two concave mirrors with a radius  
 152 of curvature of 300 mm separated by 550 mm in a Herriott con-  
 153 figuration [21] inside which a 5 mm-thick AR-coated fused silica  
 154 plate is inserted to provide nonlinearity [18]. An arrangement  
 155 of three lenses is used to match the input beam to the stationary  
 156 beam of the MPC, and the pulses are propagating through 15  
 157 roundtrips before being sent out. At the output of the MPC,  
 158 another flip mirror is used to send the pulses to a set of chirped  
 159 mirrors introducing a total group-delay dispersion of  $-16000$   
 160  $\text{fs}^2$  (spectrally broadened pulses) or directly to the frequency  
 161 tripling stage (spectrally compressed pulses). The spectral and  
 162 temporal profiles of each beamline are shown in Fig. 3. The  
 163 time-bandwidth products are 0.51, 0.43, and 0.5 for the 100 fs,  
 500 fs, and 3 ps pulses respectively.

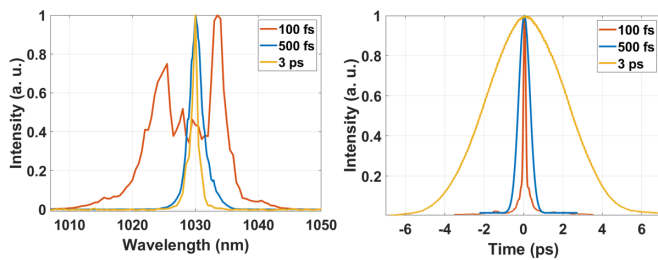


**Fig. 3.** Left: measured spectra at 1030 nm. Right: measured autocorrelation traces at 1030 nm.

164 The nonlinear crystals used in the first THG stage (all pro-  
 165 vided by Crylight) must be adapted to the three different pulse  
 166

167 durations. Each beamline of 100 fs, 500 fs and 3 ps with energies  
 168 of 150  $\mu\text{J}$ , 300  $\mu\text{J}$  and 200  $\mu\text{J}$  respectively, is therefore sent to three  
 169 parallel tripling stages. Each stage is based on SHG in a first  
 170 BBO crystal (thicknesses of 0.5, 1, and 2 mm for 100 fs, 500 fs  
 171 and 3 ps respectively), followed by SFG in a second BBO crystal  
 172 (thicknesses of 0.75, 1.5, and 2 mm for 100 fs, 500 fs and 3 ps  
 173 respectively). Before the second, gas-based THG stage, the avail-  
 174 able energies at 343 nm are 15  $\mu\text{J}$ , 30  $\mu\text{J}$ , and 30  $\mu\text{J}$  for driving  
 175 pulse durations of 100 fs, 500 fs, and 3 ps respectively. The lower  
 176 pulse energy available at 100 fs duration is due to the losses  
 177 of the chirped mirrors, and lower tripling efficiency. Although  
 178 the pulse durations at 343 nm are not measured directly, the  
 179 measured spectra indicate that the pulse durations at 1030 nm  
 180 are approximately conserved at 343 nm.

181 The second THG stage consists of a xenon-filled cell in which  
 182 the beam at 343 nm is focused, yielding a beam at 114 nm. Both  
 183 beams enter the under-vacuum detection chamber transmitted  
 184 through a lithium fluoride (LiF) window. The photon flux is  
 185 estimated by measuring the drain current from the surface of a  
 186 gold target [22] inserted just after the LiF window. Because the  
 187 work function of gold is 5.2 eV while the photon energies of the  
 188 343 nm and 114 nm light are 3.6 eV and 10.8 eV respectively,  
 189 the detection of stray light is efficiently suppressed. We have also  
 190 experimentally verified that illuminating the gold surface with  
 191 the full power at 343 nm in the absence of THG (gas cell under  
 192 vacuum), in the three different pulse duration cases, resulted in  
 193 negligible measured current. A knife edge measurement of the  
 194 114 nm beam profile, performed after a spherical mirror and a  
 195 dispersive grating to filter out the 343 nm beam, is reported in  
 196 the inset in Fig. 2.

197 We start by investigating PM effects at a driving pulse dura-  
 198 tion of 500 fs. Figure 4 shows the experimentally measured  
 199 and simulated power of the 114 nm beam as a function of gas  
 pressure, for different focused beam sizes and energies. As ob-

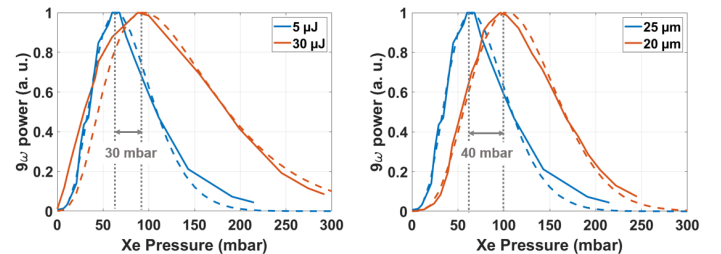


**Fig. 4.** Measured (solid line) and simulated (dashed line) power at 114 nm as a function of Xe pressure, normalized to the maximum value. Left: the beam diameter is 25  $\mu\text{m}$  (obtained using a lens with a focal length of 200 mm), the pulse energies are 5  $\mu\text{J}$  (blue) and 30  $\mu\text{J}$  (red). Right: the input energy is 5  $\mu\text{J}$ , the focused beam diameters are 20  $\mu\text{m}$  (red) and 25  $\mu\text{m}$  (blue), achieved using lenses with focal lengths of 150 mm and 200 mm, respectively.

200 served in Fig. 4 (right), the PM pressure increases for smaller  
 201 focused beam diameter, as expected for example from Eq. (5).  
 202 Fig. 4 (left) shows that the PM gas pressure also increases for  
 203 increasing input energy, as predicted by Eq. (4), because of the  
 204 onset of the ionization, causing a non-negligible contribution of  
 205 free electrons. Numerical simulations are in quantitative agree-  
 206 ment, reproducing both the PM pressure shifts and changes in  
 207 the curve shapes. In Fig. 5, the measured power at 114 nm as  
 208 a function of Xe pressure for pulse durations of 100 fs and 3  
 209

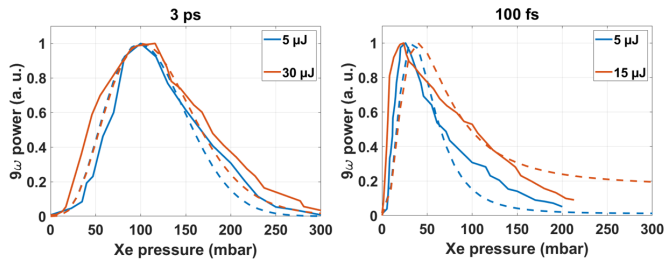


**Fig. 5.** Measured (solid line) and simulated (dashed line) power at 114 nm as a function of Xe pressure. Left: the pulse duration is 3 ps, the pulse energies are 5  $\mu\text{J}$  and 30  $\mu\text{J}$ . Right: the pulse duration is 100 fs, the pulse energies are 5  $\mu\text{J}$  and 15  $\mu\text{J}$ .

ps are presented. The focused spot diameter is 38  $\mu\text{m}$  for the 100 fs pulses and 22  $\mu\text{m}$  for the 3 ps pulses, which explains the difference in PM pressure at low pulse energies. In contrast to the data obtained for 500 fs pulses, we do not observe a PM pressure shift as a function of input pulse energy. In both cases, this can be explained by the fact that the available energies and focusing conditions lead to intensities that are below the onset of significant ionization. As discussed above, this intensity threshold is much higher for 100 fs pulses than for 3 ps pulses. The simulations are in reasonable agreement with the observed data.

We now comment on the absolute photon fluxes at 114 nm measured for the three pulse durations. To estimate them, the detected current is converted to photon flux assuming a photoelectric yield for Au of 0.08 electron per photon [22]. Figure 6 shows the photon flux as a function of input pulse energy when the pressure is fixed to the PM pressure for the maximum energy available for each beamline. At a given pulse energy, the intensity is higher for the 100 fs beamline, which translates into a higher efficiency. It is also apparent that the conversion efficiency increases with power for the 100 fs and 3 ps cases, for which ionization effects are small, which is expected for an unsaturated phase-matched third order process. However, for the 500 fs case, this efficiency appears to be almost constant. This could be caused by the fact that ionization effects are local in space and time, resulting in a constant average efficiency as the power is increased. The maximum measured photon fluxes after the LiF window at 100 fs, 500 fs, and 3 ps are  $9 \times 10^{12}$ ,  $7 \times 10^{12}$ , and  $2 \times 10^{12}$  ph/s respectively. Taking into account the transmission efficiency of the LiF window which is measured to be 30%, these photon fluxes correspond to optical-to-optical power internal conversion efficiencies of  $3 \times 10^{-5}$ ,  $1 \times 10^{-5}$ , and  $3 \times 10^{-6}$ .

In conclusion, we report a VUV table-top source at 114 nm based on cascaded THG of FTL driving pulses at 1030 nm with switchable pulse durations of 100 fs, 500 fs, and 3 ps. Assuming that the spectral widths are maintained during the wavelength conversion stages, as indicated by numerical simulations, this corresponds to energy resolutions of 15, 3, and 0.5 meV. This versatility in terms of temporal and spectral resolution, combined with a high repetition rate and sufficient photon flux should make this type of source very appealing for future tr-ARPES setups in particular in combination with high-luminosity spectrometers [23].

**Funding.** Agence Nationale de la Recherche (ANR-21-CE30-0038-SHOTIME).

**Acknowledgment.** The authors acknowledge helpful discussions

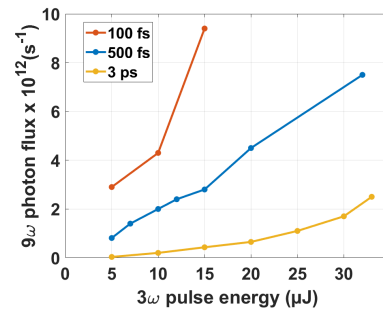


**Fig. 6.** Estimated photon flux at 114 nm as a function of input power at 343 nm for each pulse duration.

with Z. Zhao, F. Cilento and O. Tjernberg.

**Disclosures.** The authors declare no conflicts of interest.

**Data Availability Statement.** Data underlying the results presented in this article are not publicly available at this time but may be obtained from the authors upon reasonable request.

## REFERENCES

- J. A. Sobota, Y. He, and Z.-X. Shen, *Rev. Mod. Phys.* **93**, 025006 (2021).
- J. Faure, J. Mauchain, E. Papalazarou, W. Yan, J. Pinon, M. Marsi, and L. Perfetti, *Rev. Sci. Instruments* **83**, 043109 (2012).
- J. Wang, F. Chen, M. Pan, S. Xu, R. Lv, J. Liu, Y. Li, S. Fang, Y. Chen, J. Zhu, D. Zhang, T. Qian, C. Yun, K. Zhao, H. Ding, and Z. Wei, *Opt. Express* **31**, 9854 (2023).
- Q. Guo, M. Dendzik, A. Grubišić-Čabo, M. H. Berntsen, C. Li, W. Chen, B. Matta, U. Starke, B. Hessmo, J. Weissenrieder, and O. Tjernberg, *Struct. Dyn.* **9** (2022). 024304.
- R. Forbes, P. Hockett, and R. Lausten, *Opt. Lett.* **47**, 2410 (2022).
- Y. He, I. M. Vishik, M. Yi, S. Yang, Z. Liu, J. J. Lee, S. Chen, S. N. Rebec, D. Leuenberger, A. Zong *et al.*, *Rev. Sci. Instruments* **87**, 011301 (2016).
- M. H. Berntsen, O. Götberg, and O. Tjernberg, *Rev. Sci. Instruments* **82**, 095113 (2011).
- Z. Zhao and Y. Kobayashi, *Opt. Express* **25**, 13517 (2017).
- X. Zhou, S. He, G. Liu, L. Zhao, L. Yu, and W. Zhang, *Reports on Prog. Phys.* **81**, 062101 (2018).
- S. Peli, D. Puntel, D. Kopic, B. Sockol, F. Parmigiani, and F. Cilento, *J. Electron Spectrosc. Relat. Phenom.* **243**, 146978 (2020).
- J. Ward and G. New, *Phys. Rev.* **185**, 57 (1969).
- G. Bjorklund, *IEEE J. Quantum Electron.* **11**, 287 (1975).
- R. Mahon, T. McIlrath, V. Myerscough, and D. Koopman, *IEEE J. Quantum Electron.* **15**, 444 (1979).
- S. Kazamias, S. Daboussi, O. Guilbaud, K. Cassou, D. Ros, B. Cros, and G. Maynard, *Phys. Rev. A* **83**, 063405 (2011).
- S. Hädrich, J. Rothhardt, M. Krebs, S. Demmler, A. Klenke, A. Tünnermann, and J. Limpert, *J. Phys. B: At. Mol. Opt. Phys.* **49**, 172002 (2016).
- J. Schwarz, P. Rambo, and J. Diels, *Appl. Phys. B* **72**, 343 (2001).
- A. Perelomov, V. Popov, and M. Terentev, *JETP* **23**, 924 (1966).
- J. Schulte, T. Sartorius, J. Weitenberg, A. Vernaleken, and P. Russbuehldt, *Opt. Lett.* **41**, 4511 (2016).
- L. Lavenue, M. Natile, F. Guichard, X. Délen, M. Hanna, Y. Zaouter, and P. Georges, *Opt. express* **27**, 1958 (2019).
- N. Daher, F. Guichard, X. Délen, Y. Zaouter, M. Hanna, and P. Georges, *Opt. Express* **28**, 21571 (2020).
- D. Herriott, H. Kogelnik, and R. Kompfner, *Appl. Opt.* **3**, 523 (1964).
- B. Feuerbacher and B. Fitton, *J. Appl. Phys.* **43**, 1563 (1972).
- J. Zhang, Z. Chen, E. Papalazarou, M. Marsi, A. Omoumi, and J. Cailaux, "Spin and orbital texture of quantum materials from dichroism in

304 the ultrafast photoemission yield," in *Advances in Ultrafast Condensed*  
305 *Phase Physics III*, , vol. 12132 (SPIE, 2022), pp. 33–38.

## FULL REFERENCES

- 306  
307  
308  
309  
310  
311  
312  
313  
314  
315  
316  
317  
318  
319  
320  
321  
322  
323  
324  
325  
326  
327  
328  
329  
330  
331  
332  
333  
334  
335  
336  
337  
338  
339  
340  
341  
342  
343  
344  
345  
346  
347  
348  
349  
350  
351  
352  
353  
354  
355  
356  
357  
358  
359  
360  
361  
362  
363  
364  
365  
366  
367  
368  
369  
370  
371  
372  
373
1. J. A. Sobota, Y. He, and Z.-X. Shen, "Angle-resolved photoemission studies of quantum materials," *Rev. Mod. Phys.* **93**, 025006 (2021).
2. J. Faure, J. Mauchain, E. Papalazarou, W. Yan, J. Pinon, M. Marsi, and L. Perfetti, "Full characterization and optimization of a femtosecond ultraviolet laser source for time and angle-resolved photoemission on solid surfaces," *Rev. Sci. Instruments* **83**, 043109 (2012).
3. J. Wang, F. Chen, M. Pan, S. Xu, R. Lv, J. Liu, Y. Li, S. Fang, Y. Chen, J. Zhu, D. Zhang, T. Qian, C. Yun, K. Zhao, H. Ding, and Z. Wei, "High-flux wavelength tunable xuv source in the 12–40.8 eV photon energy range with adjustable energy and time resolution for tr-arpes applications," *Opt. Express* **31**, 9854–9871 (2023).
4. Q. Guo, M. Dendzik, A. Grubišić-Čabo, M. H. Berntsen, C. Li, W. Chen, B. Matta, U. Starke, B. Hessmo, J. Weissenrieder, and O. Tjernberg, "A narrow bandwidth extreme ultra-violet light source for time- and angle-resolved photoemission spectroscopy," *Struct. Dyn.* **9** (2022). 024304.
5. R. Forbes, P. Hockett, and R. Lausten, "Efficient generation of the 7th harmonic of titanium:sapphire (114.6 nm) vacuum ultraviolet pulses with 60 fs duration by non-collinear four-wave mixing in argon," *Opt. Lett.* **47**, 2410–2413 (2022).
6. Y. He, I. M. Vishik, M. Yi, S. Yang, Z. Liu, J. J. Lee, S. Chen, S. N. Rebec, D. Leuenberger, A. Zong *et al.*, "Invited article: High resolution angle resolved photoemission with tabletop 11 eV laser," *Rev. Sci. Instruments* **87**, 011301 (2016).
7. M. H. Berntsen, O. Götzberg, and O. Tjernberg, "An experimental setup for high resolution 10.5 eV laser-based angle-resolved photoelectron spectroscopy using a time-of-flight electron analyzer," *Rev. Sci. Instruments* **82**, 095113 (2011).
8. Z. Zhao and Y. Kobayashi, "Realization of a mw-level 10.7-eV ( $\lambda = 115.6$  nm) laser by cascaded third harmonic generation of a yb: fiber CPA laser at 1-mHz," *Opt. Express* **25**, 13517–13526 (2017).
9. X. Zhou, S. He, G. Liu, L. Zhao, L. Yu, and W. Zhang, "New developments in laser-based photoemission spectroscopy and its scientific applications: a key issues review," *Reports on Prog. Phys.* **81**, 062101 (2018).
10. S. Peli, D. Puntel, D. Kopic, B. Sockol, F. Parmigiani, and F. Cilento, "Time-resolved vuv arpes at 10.8 eV photon energy and MHz repetition rate," *J. Electron Spectrosc. Relat. Phenom.* **243**, 146978 (2020).
11. J. Ward and G. New, "Optical third harmonic generation in gases by a focused laser beam," *Phys. Rev.* **185**, 57 (1969).
12. G. Bjorklund, "Effects of focusing on third-order nonlinear processes in isotropic media," *IEEE J. Quantum Electron.* **11**, 287–296 (1975).
13. R. Mahon, T. McIlrath, V. Myerscough, and D. Koopman, "Third-harmonic generation in argon, krypton, and xenon: bandwidth limitations in the vicinity of Lyman- $\alpha$ ," *IEEE J. Quantum Electron.* **15**, 444–451 (1979).
14. S. Kazamias, S. Daboussi, O. Guilbaud, K. Cassou, D. Ros, B. Cros, and G. Maynard, "Pressure-induced phase matching in high-order harmonic generation," *Phys. Rev. A* **83**, 063405 (2011).
15. S. Hädrich, J. Rothhardt, M. Krebs, S. Demmler, A. Klenke, A. Tünnermann, and J. Limpert, "Single-pass high harmonic generation at high repetition rate and photon flux," *J. Phys. B: At. Mol. Opt. Phys.* **49**, 172002 (2016).
16. J. Schwarz, P. Rambo, and J. Diels, "Measurements of multiphoton ionization coefficients with ultrashort ultraviolet laser pulses," *Appl. Phys. B* **72**, 343–347 (2001).
17. A. Perelomov, V. Popov, and M. Terentev, "Ionization of atoms in an alternating electric field," *JETP* **23**, 924–934 (1966).
18. J. Schulte, T. Sartorius, J. Weitenberg, A. Vernaleken, and P. Russbuehldt, "Nonlinear pulse compression in a multi-pass cell," *Opt. Lett.* **41**, 4511–4514 (2016).
19. L. Lavenu, M. Natile, F. Guichard, X. Délen, M. Hanna, Y. Zaouter, and P. Georges, "High-power two-cycle ultrafast source based on hybrid nonlinear compression," *Opt. Express* **27**, 1958–1967 (2019).
20. N. Daher, F. Guichard, X. Délen, Y. Zaouter, M. Hanna, and P. Georges, "Spectral compression in a multipass cell," *Opt. Express* **28**, 21571–21577 (2020).
- 374  
375  
376  
377  
378  
379  
380  
381  
382
21. D. Herriott, H. Kogelnik, and R. Kompfner, "Off-axis paths in spherical mirror interferometers," *Appl. Opt.* **3**, 523–526 (1964).
22. B. Feuerbacher and B. Fitton, "Experimental investigation of photoemission from satellite surface materials," *J. Appl. Phys.* **43**, 1563–1572 (1972).
23. J. Zhang, Z. Chen, E. Papalazarou, M. Marsi, A. Omoumi, and J. Cailaux, "Spin and orbital texture of quantum materials from dichroism in the ultrafast photoemission yield," in *Advances in Ultrafast Condensed Phase Physics III*, vol. 12132 (SPIE, 2022), pp. 33–38.